Journal of Geophysical Research: Atmospheres

RESEARCH ARTICLE
10.1029/2017JD027849

Intercomparison Between VIIRS and CrIS by Taking Into Account the CrIS Subpixel Cloudiness and Viewing Geometry

Xinya Gong[1,2,3], Zhenglong Li[2], Jun Li[2], Christopher C. Moeller[2], Changyong Cao[4], Wenhui Wang[5], and W. Paul Menzel[2]

[1]College of Earth and Planetary Sciences Institute of Atmospheric Physics, Chinese Academy of Sciences, Beijing, China, [2]Cooperative Institute for Meteorological Satellite Studies, University of Wisconsin-Madison, Madison, WI, USA, [3]University of Chinese Academy of Sciences, Beijing, China, [4]Center for Satellite Applications and Research, NOAA, College Park, MD, USA, [5]Earth Resource Technology, Inc., Laurel, MD, USA

Key Points:
- CrIS subpixel cloudiness, viewing geometry, and surface types have a weak impact on VIIRS and CrIS radiance differences
- The analysis is useful for VIIRS calibration accuracy assessment and product improvement (e.g., SST)
- The methodologies and tools developed can be applied to process/reprocess data from imagers and sounders onboard the same satellite

Correspondence to:
J. Li,
jun.li@ssec.wisc.edu

Citation:
Gong, X., Li, Z., Li, J., Moeller, C. C., Cao, C., Wang, W., & Menzel, W. P. (2018). Intercomparison between VIIRS and CrIS by taking into account the CrIS subpixel cloudiness and viewing geometry. *Journal of Geophysical Research: Atmospheres*, *123*, 5335–5345. https://doi.org/10.1029/2017JD027849

Received 13 OCT 2017
Accepted 23 APR 2018
Accepted article online 4 MAY 2018
Published online 17 MAY 2018

Abstract The Cross-track Infrared Sounder (CrIS) onboard the Suomi National Polar-orbiting Partnership (SNPP) has high radiometric accuracy, which can be used to intercompare and understand the radiometric performance of the thermal emissive bands of the Visible Infrared Imaging Radiometer Suite (VIIRS) onboard the same platform. Previous studies usually selected uniform scenes to avoid potential uncertainties due to geolocation errors. This study focuses on all scenes (including nonuniform scenes), as well as CrIS subpixel cloudiness, local zenith angle and surface type, and their impacts on VIIRS/CrIS intercomparisons. A geolocation error correction scheme is applied to mitigate the geolocation mismatch between CrIS and VIIRS. Intercomparison results of three days from 19 to 21 September 2016, a quarterly warm up/cool down calibration period, show overall good agreement in terms of radiance biases (less than 0.2 K in terms of brightness temperature) between VIIRS and CrIS, for scene temperatures between 220 and 300 K; however, larger biases are evident outside of this range. The three factors—CrIS subpixel cloudiness, local zenith angle, and surface type—show weak impacts on VIIRS radiance biases. Both clear-sky and overcast conditions have slightly different radiance biases from other partially cloudy conditions because of more contributions from colder or warmer scenes. The time series show the impact of warm up/cool down and the effectiveness of the correction algorithm for reprocessing VIIRS M15 and M16 data sets. The methods and tools can be applied to monitor and validate other infrared imager/sounder duos onboard the same platform.

1. Introduction

Onboard the Suomi National Polar-orbiting Partnership (SNPP) and the coming Joint Polar Satellite Systems (JPSS) satellites, the Cross-track Infrared Sounder (CrIS; Han et al., 2013) is a Fourier transform spectrometer, providing radiance measurements of the Earth's atmosphere with measurements at high spectral (0.625–2.5 cm^{-1}) and spatial resolution (14 km at nadir). CrIS radiance measurements in either 1,305 (normal mode) or 2,211 (full spectral resolution mode) channels cover three wavelength ranges: long-wave infrared (LWIR; 9.14–15.38 μm), midwave infrared (5.71–8.26 μm), and shortwave infrared (3.92–4.64 μm). Along with the Atmospheric InfraRed Sounder (AIRS; Chahine et al., 2006) on the Aqua satellite and the Infrared Atmospheric Sounding Interferometer (IASI; Chalon et al., 2001; Collard & McNally, 2009) on the European MetOp-A/B satellites, CrIS provides needed information about global atmospheric profiles with high vertical resolution for numerical weather prediction models (Cucurull et al., 2014; Joo et al., 2013; Wang, Li, et al., 2017). Calibration and validation of the CrIS Sensor Data Records (SDRs) are performed before (Zavyalov et al., 2011) and after the launch (Han et al., 2013; Zhou et al., 2016) in order to determine the instrument noise characteristics (Zavyalov et al., 2013), the spectral/radiometric performance (Strow et al., 2013; Tobin, Revercomb, Knuteson, Best, et al., 2013; Tobin, Revercomb, Knuteson, Taylor, et al., 2013; Wang et al., 2015), and the geolocation accuracy (Wang et al., 2013; Wang, Zhang, et al., 2017).

The Visible Infrared Imaging Radiometer Suite (VIIRS) onboard the same platform is a filter radiometer with 17 visible/near-infrared and 5 infrared (IR) spectral bands between 0.412 and 12.01 μm, collecting imagery and radiometric data of the Earth and its atmosphere (Cao et al., 2014; De Luccia et al., 2011; Hillger et al., 2013). With its high radiometric accuracy and spatial resolution (750 m for moderate-resolution bands [M bands] and 375 m for imaging resolution bands [I bands] at nadir), VIIRS continues the heritage measurements

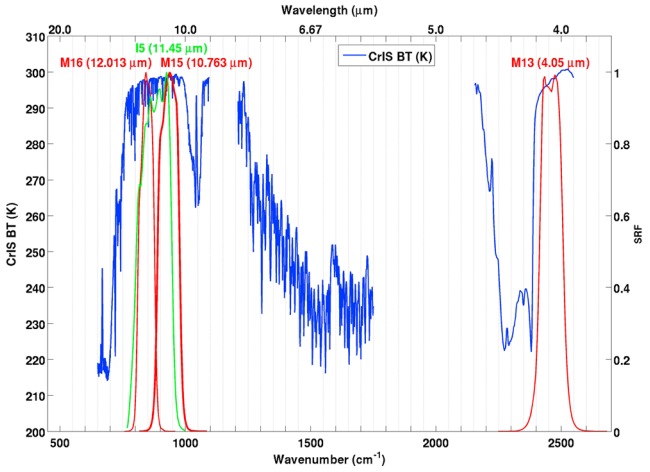

Figure 1. The spectral response functions of VIIRS bands M13, M15, M16 (red), and I5 (green) overlaid on a CrIS brightness temperature observation (blue, unit: K) from a randomly selected CrIS field of view.

from the Advanced Very High Resolution Radiometer (AVHRR) on Polar Operational Environmental Satellites (POES), the Operational Linescan System (OLS) on Defense Meteorological Satellite Program (DMSP; Elvidge et al., 2013), and the Moderate Resolution Imaging Spectroradiometer (MODIS) on the Terra and Aqua satellites (Cao et al., 2013; Li et al., 2016; Liang & Ignatov, 2013; Madhavan et al., 2016). More than 20 Environmental Data Records (EDR), such as sea surface temperature (SST), cloud properties, and fires, are produced from the calibrated VIIRS SDR (Cao et al., 2013; Liu et al., 2013; Xiong et al., 2014).

As CrIS and VIIRS are on the same SNPP platform, they provide an opportunity for comprehensive intercomparisons of each other throughout SNPP's lifetime. A methodology and tool have been developed to collocate different satellite measurements (Nagle & Holz, 2009). In addition, an improved technique has been developed by Wang et al., 2016 to allow fast and accurate collocation of VIIRS with CrIS. Previous work has pointed out the advantages of using VIIRS and CrIS for intercalibrations (Moeller et al., 2013; Tobin, Revercomb, Knuteson, Best, et al., 2013; Wang et al., 2012). However, the impacts of CrIS subpixel clouds, local zenith angle (LZA), and surface type on the VIIRS/CrIS intercomparison were not studied. In addition, during the unsteady state of quarterly warm up/cool down (WUCD) periods, the performance of the thermal emissive bands (TEBs) and the effect on the correction algorithms (Cao et al., 2017; Choi et al., 2016) need further independent assessment.

It should be noted that the CrIS radiometric accuracy is about 0.2–0.3 K (Han et al., 2013) while the VIIRS is 0.1 K under nominal operation based on prelaunch tests (Cao et al., 2013). With the stable calibration of CrIS (Strow et al., 2013), it can be used to study and better understand the VIIRS radiometric performance. Since this study will focus on the radiance differences between VIIRS and CrIS, it is difficult to tell the absolute radiometric accuracy of VIIRS SDRs or how it will affect the downstream EDR products. Instead, this study provides a chance to better understand the VIIRS radiometric accuracy in various conditions, such as scene temperature, cloudiness, LZA, and surface types. This knowledge will help identify problems in the future if abnormal differences between VIIRS and CrIS are observed.

In this paper, the data and methodology are presented in sections 2 and 3; the statistics analysis and results are shown in section 4; the WUCD time series results are shown in section 5; finally, the summary and a description of future work are given in section 6.

2. Data

For this study, the following data from 0000 UTC of 19 September 2016 to 2359 UTC of 21 September 2016 have been used: CrIS SDR radiances (SCRIS) and geolocation (GCRSO) information, VIIRS SDR radiances of TEBs (SVM12–16 and SVI05) and geolocation (GMODO) information, and VIIRS cloud mask product (IICMO, later replaced by VICMO). The CrIS SDR data are provided by the Atmosphere Science Investigator-led Processing Systems (SIPS) of the National Aeronautics and Space Administration, located at the University of Wisconsin-Madison, Space Science and Engineering Center (http://sips.ssec.wisc.edu). The VIIRS SDR and cloud mask product are provided by the Comprehensive Large Array-data Stewardship System (CLASS) of the National Oceanic and Atmospheric Administration (NOAA; https://www.class.ngdc.noaa.gov). The reprocessed VIIRS SDR data were provided by the NOAA/National Environmental Satellite, Data, and Information Service/Center for Satellite Applications and Research VIIRS SDR team.

3. Methodology

3.1. VIIRS/CrIS Collocation

Previous studies show that the CrIS can be used to evaluate the calibration of those VIIRS TEBs, which have complete (i.e., M15, M16, and I5) or nearly complete (i.e., M13) coverage by the CrIS spectrum (Moeller

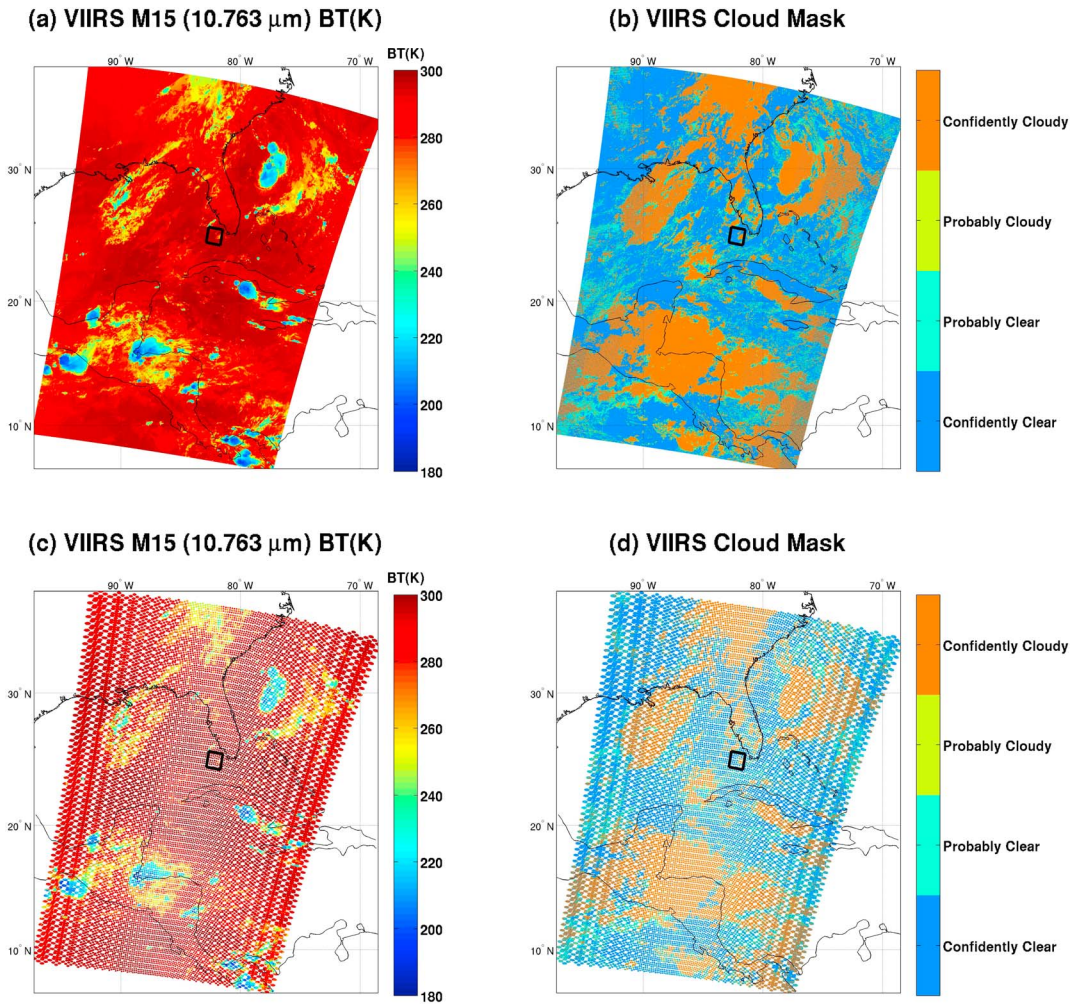

Figure 2. VIIRS M15 BTs (unit: K) (a) before and (c) after collocation, and VIIRS cloud mask (b) before and (d) after collocation, with one CrIS granule over the southeastern part of North and Central America at 0716 UTC on 19 September 2016. The definition of "confident cloudy," "probably cloudy," "probably clear," and "confident clear" comes from the VIIRS retrieval products. The black square box denotes the area shown in Figure 3.

et al., 2013; Tobin, Revercomb, Knuteson, Best, et al., 2013; Wang et al., 2012). Figure 1 shows the spectral response functions (SRFs) of VIIRS bands M13, M15, M16, and I5 overlaid on a CrIS brightness temperature (BT) spectrum for a randomly selected CrIS field of view (FOV). This study will focus on those four VIIRS spectral bands.

Using the imager/sounder collocation tool developed by the SIPS team (Nagle & Holz, 2009), the indices and weights of VIIRS pixels that fall within each CrIS FOV (coincident in time and space) are found for the M bands. Globally, for the three days from 19 to 21 September 2016, more than 8,000,000 CrIS FOVs are successfully collocated with VIIRS pixels. For VIIRS band I5 (11.45 μm) with higher spatial resolution, the number of matchups with each CrIS FOV is four times higher than that for the M bands. Figure 2 shows the VIIRS M15 BTs and VIIRS cloud mask of one CrIS granule over the southeastern part of North and Central America at 0716 UTC on 19 September 2016 both before and after the collocation. The holes after the collocation are due to the data gap between CrIS FOVs. For each VIIRS band, the CrIS radiances are spectrally convolved using the corresponding VIIRS SRF, and the VIIRS radiances are spatially averaged over each collocated CrIS FOV. For all four VIIRS spectral bands, only the in-band response is considered, since the impact from the out of band (OOB) response is small (Moeller et al., 2013). The entire process is performed in the radiance space, including calculating the mean bias and standard deviation (STD). In the end, these values are converted to BTs using Planck functions. In this study, the radiance biases and STD refer to BT biases and STD.

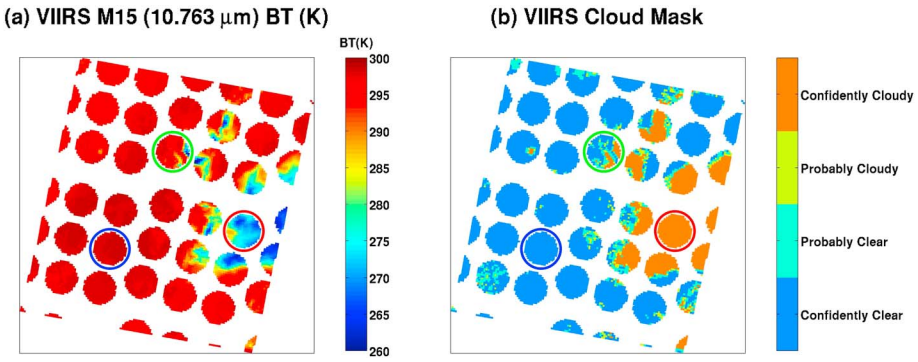

Figure 3. (a) VIIRS M15 BTs (unit: K) and (b) VIIRS cloud mask after collocation with CrIS FOVs of the area outlined by the black square in Figure 2. The blue, green, and red circles represent one example each for clear sky, partially cloudy, and overcast FOVs, respectively.

3.2. CrIS Subpixel Cloudiness and Surface Type

The VIIRS cloud mask serves as an intermediate product between the production of VIIRS SDRs and the downstream EDRs both of which depend upon the cloud mask output (Kopp et al., 2014). The cloud detection algorithm uses many of the available bands, with the results from all cloud tests combined to create the cloud confidence analysis (Hutchison et al., 2012). Based on the overall cloud-free probability, the VIIRS pixels are categorized as "confidently cloudy," "probably cloudy," "probably clear," and "confidently clear" in the M band pixel space. The algorithm has been discussed extensively in the VIIRS cloud mask Algorithm Theoretical Basis Document (ATBD; National Aeronautics and Space Administration, 2013).

Using the high spatial resolution VIIRS cloud mask product, the CrIS subpixel characterization (e.g., cloud presence and surface type) can be derived using the methodology developed by Li et al. (2004). For the intercomparisons in this paper, both confidently clear and probably clear retrievals from the VIIRS cloud mask are treated as clear pixels, and both confidently cloudy and probably cloudy retrievals from the VIIRS cloud mask are treated as cloudy pixels. The CrIS subpixel cloudiness is calculated as the percentage of VIIRS cloudy pixels passing quality controls out of all collocated VIIRS pixels. Figure 3 shows the CrIS subpixel characterization from the VIIRS M15 BTs and cloud mask of the area outlined by the black square box in Figure 2. The blue, green, red circles show one example each for clear sky, partially cloudy, and overcast FOVs, respectively.

The CrIS surface type is derived from the high spatial resolution VIIRS land/water mask product by calculating the percentage of the VIIRS pixels over "seawater" in each CrIS FOV. If the percentage is equal to 100%, the CrIS surface type is defined as "ocean"; if the percentage is equal to 0%, the CrIS surface type is defined as "land"; for anything in between, the CrIS surface type is defined as "coastal." As a result, all surface types over land such as deserts, land, lakes, and coastal near inland lakes from the VIIRS land/water mask product are treated as land for the CrIS FOVs.

3.3. CrIS Geolocation Error Correction

According to Wang, Zhang, et al. (2017), the CrIS has substantial geolocation errors compared with VIIRS; the errors are as large as 4.7 km in the cross-track direction and 1.3 km in the along-track direction at scan edges. These errors cause geolocation mismatches between CrIS and VIIRS. An SDR software update has been implemented to fix this geolocation issue since June 2017 using the technique developed by Wang, Zhang, et al. (2017). Because the time period selected for this study has not been corrected for such errors, we have implemented a simplified correction scheme. While Wang, Zhang, et al. (2017) corrects the CrIS geolocation so that it has no geolocation error compared with VIIRS, our simplified scheme focuses on finding the correct collocated VIIRS pixels for each CrIS FOV. Take CrIS field-of-regard (FOR, each FOR contains 3 by 3 FOVs) 30 as an example. The mean cross-track geolocation error of 4.7 km is about the size of six VIIRS pixels. Note that the VIIRS pixel size is about 0.8 km at the scan angle of 48.3° for CrIS FOR 30. Instead of correcting the CrIS geolocation to account for the 4.7 km error, the indices of VIIRS pixels collocated with each CrIS FOV in FOR 30 are shifted toward the scan edge by six. Other FORs are processed in a similar way, in both cross-track and along-track directions. The estimated geolocation errors shown in Figure 8 in Wang, Zhang, et al. (2017) are used to

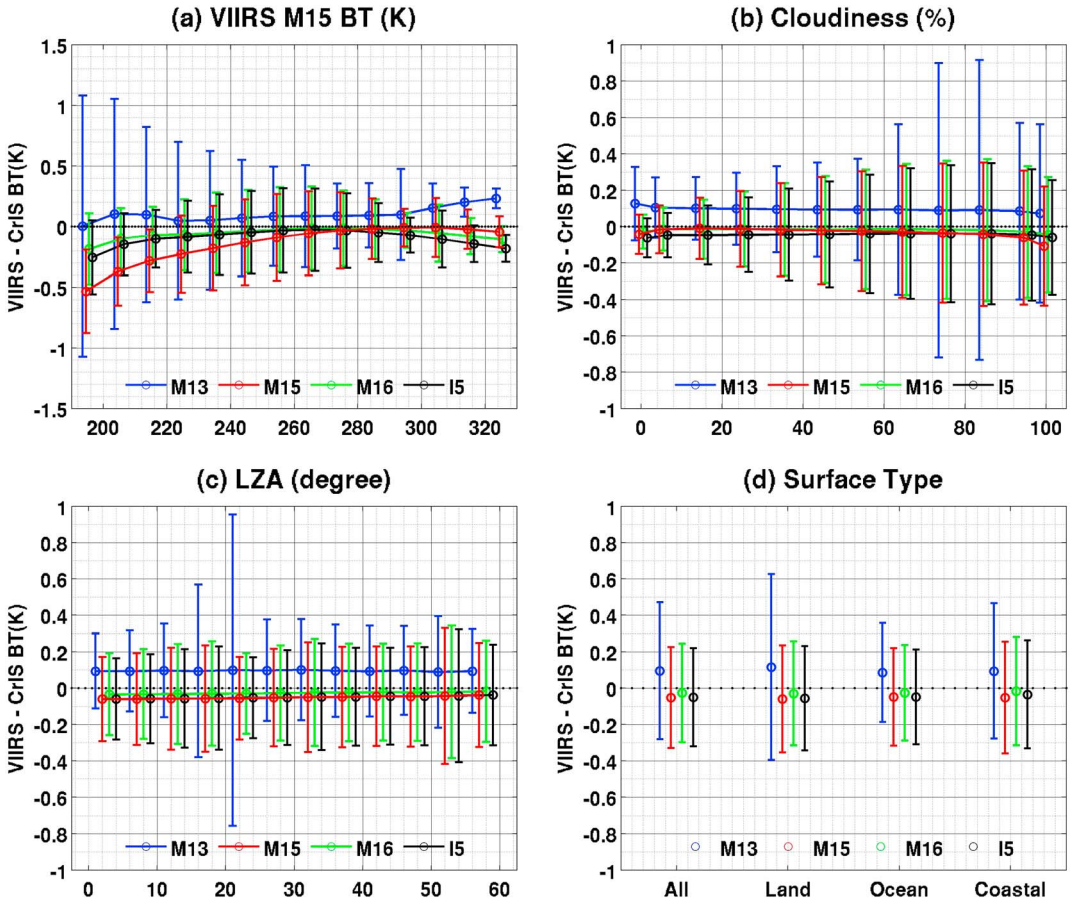

Figure 4. The radiance biases (K) and STD (bars) of radiance differences between VIIRS and CrIS (VIIRS-CrIS) for VIIRS TEBs M13, M15, M16, and I5 as functions of (a) VIIRS M15 BT (K), (b) CrIS subpixel cloudiness (%), (c) local zenith angle (LZA, °), and (d) surface type (all, land, ocean, or coastal) for 19 to 21 September 2016 with more than 8,000,000 VIIRS/CrIS matchups of all scenes.

determine how many VIIRS pixels to shift and which direction to shift, for each CrIS FOR. Note that, as both fly on SNPP, the VIIRS and CrIS have the same directions in the along-track axis, but opposite scan directions in the cross-track axis (Wang et al., 2012). Therefore, in the cross-track direction, the shifting direction of VIIRS pixel indices should be reversed accordingly. In this way, the impact of CrIS geolocation errors discovered by Wang, Zhang, et al. (2017) can be greatly mitigated. The results presented in sections 4 and 5 are after this simplified geolocation correction.

4. Statistics Analysis and Results

4.1. Analysis and Results

All the VIIRS/CrIS matchups in the three-day ensemble are classified into different categories according to (1) VIIRS M15 BT, or the scene temperature (200–320 K with an interval of 10 K); (2) CrIS subpixel cloudiness (0%–100% with an interval of 10%); (3) LZA (0°–60° with an interval of 5°); and (4) surface type (the "all" type includes all land, ocean, and coastal together). For each VIIRS spectral band and each category, the bias and STD of radiance differences between VIIRS and CrIS (VIIRS-CrIS) are calculated. The smaller bias and STD indicate a better agreement between VIIRS and CrIS. The radiance bias and STD are converted to BT values using Planck functions for easy understanding. The radiance bias shows the radiometric accuracy of VIIRS observations compared with CrIS, and the STD reflects the uncertainty of the VIIRS radiometric accuracy.

In previous studies, similar methods and tools have been used for intercomparisons between different IR sensors (Moeller et al., 2013; Tobin, Revercomb, Knuteson, Best, et al., 2013; Wang et al., 2012). The uniqueness of this work is it focuses on the CrIS subpixel characteristics and their impacts on the VIIRS radiometric accuracy

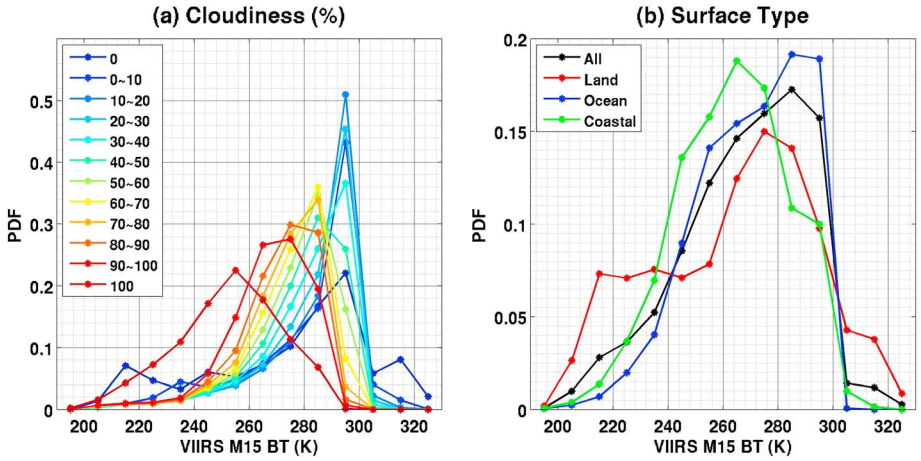

Figure 5. The probability density distributions (PDFs) of scene temperatures (VIIRS M15 BT) for different (a) CrIS subpixel cloudiness and (b) surface types for 19 to 21 September 2016.

for all scenes, including both uniform and nonuniform scenes. With more than 8,000,000 VIIRS/CrIS matchup ensembles for all scenes, it is possible to draw meaningful statistics with a limited period of time. The three-day ensemble results are shown in Figure 4.

4.1.1. Scene Temperature

For scene temperatures between 220 and 300 K, the CrIS and VIIRS show overall good agreement in terms of absolute radiance biases (less than 0.1 K for M13, M16, and I5, and less than 0.2 K for M15). In fact, the biases for all bands at all scene temperatures are within the VIIRS radiometric requirements (see Table 2 in Moeller et al., 2013). Compared with CrIS, the VIIRS mean radiance is slightly warmer for M13, and slightly colder for LWIR bands M15, M16, and I5. As scene temperatures decrease ($<$220 K), the LWIR bands show radiance biases becoming more negative. Particularly for band M15, the bias reaches $-$0.5 K with scene temperatures below 200 K. As scene temperatures increase ($>$300 K), the biases appear to deviate from those in between 220 and 300 K for all bands as well, although not as significantly as below 220 K. These results are consistent with previous studies (Moeller et al., 2013; Tobin, Revercomb, Knuteson, Best, et al., 2013; Wang et al., 2012), where uniform scene are used. Compared with other spectral bands, the M13 appears to have significantly larger STDs at cold scene temperatures. The reason is that the Planck Function has a very strong exponential relationship between BT and radiance for M13 at cold scenes.

4.1.2. CrIS Subpixel Cloudiness, LZA, and Surface Type

From Figure 4b, from clear sky to overcast, the radiance biases are all somewhat flat, especially for partially cloudy conditions, indicating a weak impact from the cloudiness. This result is surprising since the cloudy scenes tend to have cold scene temperatures and larger radiance biases (more negative) for M15, M16, and I5, according to Figure 4a. To investigate that result, the probability density functions (PDFs) of scene temperature (M15 BT) for different cloudiness levels are examined. As shown in Figure 5a, the partially cloudy classes as well as overcast conditions have unimodal PDFs. As expected, the PDFs shift toward the colder side as the cloudiness increases, indicating that the mean scene temperature decreases with increased cloudiness. For partially cloudy classes, the mean scene temperature gradually changes from 285 to 268 K as cloudiness increases, with the largest drop of 3.5 K from the class of 80–90% to that of 90–100%. From Figure 4a, all four bands have radiance biases that are relatively small and flat between those two values. As a result, the cloudiness impact on radiance biases is weak for partially cloudy conditions. However, as the cloudiness increases from 90 to 100% cloudy to overcast, the mean scene temperature dramatically drops from 268 to 255 K. This change triggers a drop of 0.05 K in the M15 radiance bias in Figure 4b. A smaller impact is seen for the other three VIIRS spectral bands.

In addition, for clear skies, the scene temperature has a triple-mode PDF, with about 8% of observations having scene temperatures below 220 K and 16% of observations having scene temperatures warmer than 300 K. From Figure 4a, for M15, M16, and I5, more contributions from both tails make the VIIRS radiance biases more negative, thus additional negative radiance biases compared with the class of 0–10% partially cloudy, and for M13, more contributions from the warm tail than the cold one make the VIIRS radiance bias warmer

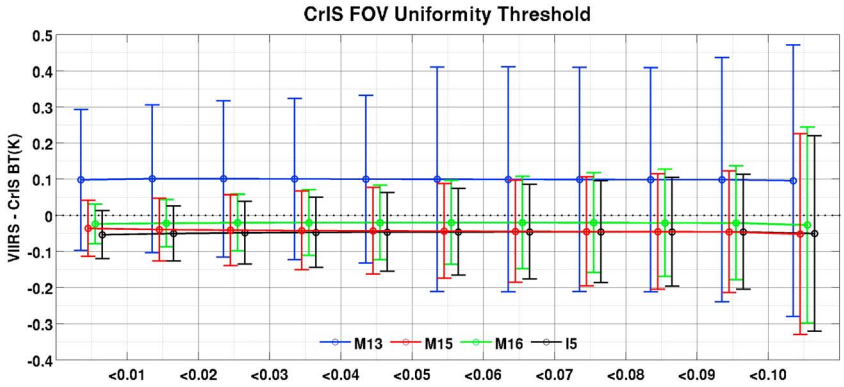

Figure 6. The radiance biases (K) and STD (bars) of the radiance differences between VIIRS and CrIS (VIIRS-CrIS) for VIIRS TEBs M13, M15, M16, and I5 as a function of uniformity indices for 19 to 21 September 2016. The last column represents results without uniform tests.

than the partially cloudy conditions, thus leading to an additional positive radiance bias. These results indicate that the CrIS subpixel cloudiness has only a weak impact on VIIRS radiance biases. The impact is more substantial for both clear sky and overcast than partially cloudy. Therefore, when characterizing the VIIRS radiometric accuracy using CrIS, the subpixel cloudiness is a minor factor. As for the uncertainty of radiometric accuracy, the subpixel cloudiness has a substantial impact with the STD increasing as cloudiness increases from clear sky to overcast. The M13 has substantially larger STDs for cloudiness levels of 60%–90% than other classes due to sun glint causing extremely large radiance differences for some FOVs. More details about this effect are provided in section 4.2.2.

From Figure 4c, LZA has a subtle impact on radiance biases; as LZA increases from zero to maximum value, the PDFs of the scene temperature change only slightly (not shown), and the mean scene temperature decreases about 3 K from 272 to 269 K. This small change in mean scene temperature has little impact on the radiance biases. As a result, the radiance biases for all four spectral bands are quite flat. However, very small radiance bias increases (about 0.02 K) are noted from nadir to the scan edge for M15, M16, and I5. Similar results were reported previously (Moeller et al., 2013; Tobin, Revercomb, Knuteson, Best, et al., 2013). As for M13, LZA has no obvious systematic impact on the radiance bias. While the STD varies with LZA, there is no obvious pattern found on the STD variations. Note that exceptionally larger STDs are observed for LZA between 15° and 25° than other classes due to the sun glint effect mentioned above. Further discussions are provided in section 4.2.2.

For all four VIIRS spectral bands, surface types have a subtle impact on the VIIRS radiance biases except for M13 over land (Figure 4d); there are no distinct differences in the radiance biases. This is reasonable because the warmest scene of ocean has a mean scene temperature of 272 K, only slightly warmer than the scene of land (268 K) and coastal areas (266 K). But there is a substantial impact on M13, in terms of both radiance bias and STD. From Figure 5b, about 10% of the CrIS FOVs over land have scene temperatures colder than 220 K and 9% warmer than 300 K. The significant contributions from both tails make the M13 radiance bias slightly larger, and the STD substantially larger than other surface types.

4.2. Discussion

4.2.1. Uniformity

In most previous studies (Moeller et al., 2013; Tobin, Revercomb, Knuteson, Best, et al., 2013; Tobin et al., 2016; Wang et al., 2012), uniform scenes are usually selected to avoid potential uncertainties caused by geolocation errors and the collocation method. While the unique aspect of this study is the focus on the CrIS subpixel impact, it is important to include both uniform and nonuniform scenes, and understand how the results are affected by the uniformity. For that, the uniformity index of each CrIS FOV is defined as the ratio of the STD of the VIIRS radiances to the mean radiance within that CrIS FOV (Wang et al., 2012). Different uniformity threshold values from 0.01 to 0.1 are used to screen out the nonuniform FOVs. The results in Figure 6 show that the uniformity has little impact on the radiance biases, as long as a statistically large sample is used for analysis. The results are also consistent with previous studies (Tobin, Revercomb, Knuteson, Best, et al., 2013; Tobin et al., 2016). However, the uniformity does have a substantial impact on the STDs. The first

column of Figure 6, with a threshold of 0.01 to screen out nonuniform CrIS FOVs, has the least impact from the nonuniformity. Using that as a baseline, the STD of all scenes (the last column of Figure 6) explained by the nonuniformity is more than 48%, 72%, 80%, and 75% for M13, M15, M16, and I5, respectively. These results indicate that the scene uniformity has little impact on the radiance biases, but substantial impact on the uncertainty of the radiometric accuracy. Therefore, nonuniform scenes may be included to characterize VIIRS radiometric accuracy using the CrIS measurements when VIIRS and CrIS are accurately collocated.

4.2.2. Residual Geolocation Error

The geolocation correction is important for VIIRS/CrIS intercomparisons (Tobin et al., 2016; Wang, Zhang, et al., 2017). As mentioned, the results presented in Figure 4 are after the simplified geolocation error correction. Compared with results without the geolocation correction, the STDs for all scenes are reduced by 18%, 38%, 39%, and 38% for M13, M15, M16, and I5, respectively, but there is little change in the radiance biases. From the last column in Figure 6, the STD for all scenes without the uniformity test is 0.27 K for I5, which is comparable to the results from Figure 15 in Wang, Zhang, et al. (2017). This result indicates that the simplified correction method used in this study is able to mitigate the geolocation errors identified by Wang, Zhang, et al. (2017). However, the more accurate correction scheme from Wang, Zhang, et al. (2017) should be used if further minimization of potential uncertainties caused by geolocation errors is desired. In this simplified correction scheme, no correction is performed if the geolocation error identified by Wang, Zhang, et al. (2017) is less than half the pixel size of VIIRS.

While results presented in this study indicate that impact from the residual geolocation error is small, the abnormally large STDs for band M13 in Figure 4b for partially cloudy classes 60–90% and Figure 4c between LZA of 15°–25° could be partially caused by the residual geolocation error. A close examination of the M13 BT reveals that those large STDs are caused by tens of samples with abnormally large radiance differences between VIIRS and CrIS. Those large radiance differences are associated with sun glint, which causes excessive solar reflection by clouds, and thus abnormally large shortwave infrared BT values. It is important to point out that the CrIS SDR does not mask those FOVs as affected by sun glint. However, three facts verify that those observations are affected by the sun glint over clouds: (1) The LZA is similar to the solar zenith angle, (2) the azimuth angle difference between the satellite and the Sun is about 180°, and (3) they are cloud affected. From the Planck function, the radiance of M13 increases exponentially with BT. When collocating VIIRS with CrIS FOVs, including or excluding a few VIIRS pixels with very large radiance values (as large as 500 K) could result in a large discrepancy (as large as 50 K) when calculating the mean M13 radiance over the CrIS FOV. This means the residual geolocation error could greatly amplify the M13 discrepancy under sun glint conditions. Removing those observations strongly affected by sun glint will bring the STDs to normal for partially cloudy classes 60–90% and LZA of 15°–25°. This is not a problem for LWIR bands like M15, M16, and I5, because (1) they are not affected by solar reflection so they do not have many pixels with extremely large BT values and (2) the Planck radiances of these three bands change less exponentially with BT than M13.

4.2.3. Other Factors

As mentioned, the OOB response is not considered when converting the CrIS radiances to VIIRS spectrums using SRFs. However, these OOB errors are unlikely to change the overall results presented in this study. According to Moeller et al. (2013), the influence of VIIRS OOB response can be neglected for M15, M16, and I5, whose OOB errors are less than 0.04, 0.005, and 0.001 K, respectively. M13 has a slightly larger OOB error reaching 0.1 K at scene temperatures of 205 K. Overall, the OOB impact on the analysis of Figure 4a is small. Similarly, the OOB impact on the analysis of cloudiness, LZA, and surface type is also small compared with the results shown in Figures 4b–4d.

The possible impact of bow tie effect and aggregation schemes (Gladkova et al., 2016) was also examined. For VIIRS scan angles less than 32°, three detector footprints are aggregated in the cross-track direction to form one VIIRS pixel. For scan angles between 32° and 45°, two footprints are aggregated, while no aggregation is needed for pixels with scan angles greater than 45°. This aggregation scheme produces similar pixel sizes along the VIIRS cross-track direction, but results in discontinuities at the two aggregation change angles. To study the impact of these discontinuities on our analysis, the mean CrIS cloudiness as a function of LZA and FOR number in the scan is calculated. And the results show no obvious impact from the bow tie effect on the calculated CrIS cloudiness (not shown), as well as no discontinuity around the two scan angles of 32° or 45°. Consequently, the bow tie effect and the aggregation scheme have little impact on the analysis presented here.

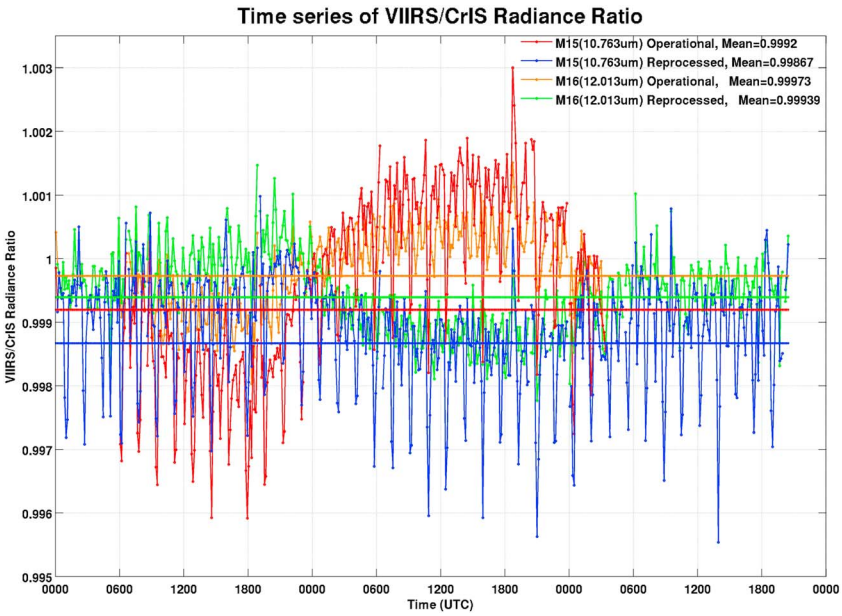

Figure 7. The time series of the mean radiance ratio (VIIRS/CrIS) for both the operational (M15, red, and M16, orange) and the reprocessed (M15, blue, and M16, green) SDR from 19 to 21 September 2016.

5. Time Series During WUCD

Periodically, the VIIRS sensor goes through an on-orbit calibration evaluation during a blackbody temperature WUCD. During a WUCD, the blackbody operating temperature is cycled through a range of 265 to 315 K. This procedure has revealed a bias dependence (about 0.1 K) in the TEBs on the blackbody operating temperature (Cao et al., 2017). This dependence leads to unexpected biases in some of the retrieval products, such as SST (about 0.3 K of bias is found from the VIIRS SST). To address this problem, Cao et al. (2017) introduced a correction algorithm (L-trace algorithm) to the calibration parameter (F-factor) in the VIIRS SDR radiance calculation. In this study, the comparison with CrIS radiances is carried out to understand the behavior of the LWIR bands M15 and M16 and the corrective effects of the reprocessing algorithm in response to the WUCD event in September 2016.

Due to the small magnitude of the bias dependence, only clear-sky CrIS FOVs over ocean are selected for evaluation and analysis as they have more uniform scenes and are less affected by cloudiness. Figure 7 shows the radiance ratio of VIIRS to CrIS for M15 and M16 from both the operational SDR data and the reprocessed data in a time series from 19 to 21 September 2016 (a WUCD period). Each dot in the time series represents the mean radiance ratio over one 8-min CrIS granule. The operational SDR shows a wave-like pattern for both bands as a result of the WUCD impact. The radiance ratio decreases during the warm up phase (from 06 UTC to 21 UTC of 19 September), then increases during the cool down phase (from 21 UTC of 19 September to 21 UTC of 20 September), and returns to normal on the third day. The radiance ratio biases introduced during the WUCD exercise are as large as ±0.2% (equivalent to ±0.1 K) for band M15. The equivalent BTs converted from the radiance biases in the time series (not shown) have similar patterns to the radiance ratio. After reprocessing, the radiance ratios are successfully modified by removing most of the systematic wave-like variation caused by the WUCD. The regular spikes (large cold biases) appearing approximately every 100 min in the time series (both before and after reprocessing) are due to those very cold scenes in Antarctica. In addition, the irregular spikes (extremely large warm or cold biases) are due to the small sample size (few CrIS granules).

6. Summary and Future Work

The CrIS with its high radiometric accuracy flies together with VIIRS on the SNPP satellite, providing a great opportunity to intercompare and calibrate the radiometric accuracy of the latter. Previous studies usually selected uniform scenes to avoid potential uncertainties due to geolocation errors. This study focuses on

all scenes, including both uniform and nonuniform scenes, as well as CrIS subpixel cloudiness, LZA and surface type, and their impacts on VIIRS/CrIS intercomparisons. In this study, the three days of global ensemble data (from 19 to 21 September 2016, a WUCD period), with more than 8,000,000 VIIRS/CrIS matchups, are used for the analysis. Results show a close agreement of less than 0.2 K between the VIIRS and CrIS biases for scene temperatures between 220 and 300 K. The biases increase modestly for scene temperatures outside of this range, especially for very cold scenes. The CrIS subpixel cloudiness, LZA, and surface types have weak to subtle impacts on the VIIRS radiance biases; all four VIIRS spectral bands have relative flat radiance biases as functions of the three factors. Both clear-sky and overcast conditions have slightly different radiance biases from other partially cloudy conditions because colder or warmer scene temperatures are used for those conditions. These results indicate that scenes affected by clouds, with large zenith angles, or with nonuniform surface conditions, may be included to characterize VIIRS radiometric accuracy using CrIS when they are accurately collocated.

A simplified correction scheme is applied to mitigate the geolocation error between VIIRS and CrIS. The correction significantly reduces the STD of the radiance differences between VIIRS and CrIS by 18%, 38%, 39%, and 38% for M13, M15, M16, and I5, but it has little impact on the radiance biases. Similarly, the uniformity is found to have little impact on radiance biases, but substantial impact on the STDs. Abnormally large M13 STDs are seen for zenith angles between 15° and 25° and partially cloudy conditions with 60–90% cloudiness. These values are found to be associated with sun glint, where both VIIRS and CrIS have abnormally warm BT values (VIIRS could be as warm as 500 K, with a discrepancy as large as 50 K comparing to the convolved CrIS). With residual geolocation errors, mistakenly including or excluding such observations may lead to significant differences between VIIRS and CrIS. The time series analysis of M15 and M16 during the WUCD period shows that the L-trace algorithm is able to remove the wave-like bias dependence. Since the VIIRS calibration performance is essential to product quality (Xiong et al., 2016), for example, the performance of M15 and M16 bands is important for SST and land surface temperature applications, while the performance of M13 band is critical for fire detection applications, especially when considering the human factors in fire monitoring, warning, and forecasting, which was first developed by Lu et al. (2016); the technical approaches developed in this manuscript are useful for evaluating and monitoring the VIIRS calibration performance. The methodologies and tools developed can also be applied to monitor and intercompare other imagers with advanced IR sounders onboard the same platforms, such as VIIRS with CrIS on the coming JPSS series and the Advanced Geosynchronous Radiation Imager (AGRI) with the Geosynchronous Interferometric InfraRed Sounder (GIIRS) on the FengYun-4 geostationary satellite series (Yang et al., 2017). For future work, more analysis of cloud types (e.g., cloud top height and cloud optical thickness), landscape, and CrIS FOVs' spatial resolution (simulation) will be explored.

Acknowledgments

This work is supported by the VIIRS SDR science team through the NOAA cooperative agreement program NA15NES4320001 and the Chinese Scholarship Council (CSC), supporting one of the coauthors (X. Gong) for her visit to the Cooperative Institute for Meteorological Satellite Studies at the University of Wisconsin-Madison. The CrIS SDR data used in this study can be obtained from NASA SIPS at University of Wisconsin-Madison (http://sips.ssec.wisc.edu/), and the VIIRS data used in this study can be obtained from NOAA CLASS (www.class.noaa.gov). The views, opinions, and findings contained in this report are those of the authors and should not be construed as an official National Oceanic and Atmospheric Administration's or U.S. government's position, policy, or decision.

References

Cao, C., De Luccia, F. J., Xiong, X., Wolfe, R., & Weng, F. (2014). Early on-orbit performance of the Visible Infrared Imaging Radiometer Suite onboard the Suomi National Polar-Orbiting Partnership (S-NPP) satellite. *IEEE Transactions on Geoscience and Remote Sensing*, *52*(2), 1142–1156. https://doi.org/10.1109/TGRS.2013.2247768

Cao, C., Wang, W., Blonski, S., & Zhang, B. (2017). Radiometric traceability diagnosis and bias correction for the Suomi NPP VIIRS long-wave infrared channels during blackbody unsteady states. *Journal of Geophysical Research: Atmospheres*, *122*, 5285–5297. https://doi.org/10.1002/2017JD026590

Cao, C., Xiong, J., Blonski, S., Liu, Q., Uprety, S., Shao, X., et al. (2013). Suomi NPP VIIRS sensor data record verification, validation, and long-term performance monitoring. *Journal of Geophysical Research: Atmospheres*, *118*, 11,664–11,678. https://doi.org/10.1002/2013JD020418

Chahine, M. T., Pagano, T. S., Aumann, H. H., Atlas, R., Barnet, C., Blaisdell, J., et al. (2006). AIRS: Improving weather forecasting and providing new data on greenhouse gases. *Bulletin of the American Meteorological Society*, *87*(7), 911–926. https://doi.org/10.1175/BAMS-87-7-911

Chalon, G., Cayla, F., & Diebel, D. (2001). 'IASI: an advanced sounder for operational meteorology'. In: *Proceedings of the 52nd Congress of IAF* (pp. 1–5). Toulouse, France.

Choi, T. J., Cao, C., & Weng, F. (2016). S-NPP VIIRS thermal emissive band gain correction during the blackbody warm-up-cool-down cycle. In *Earth Observing Systems XXI* (Vol. 9972, p. 99721J). International Society for Optics and Photonics. Retrieved from https://www.spiedigitallibrary.org/conference-proceedings-of-spie/9972/1/S-NPP-VIIRS-thermal-emissive-band-gain-correction-during-the/10.1117/12.2236995.full

Collard, A. D., & McNally, A. P. (2009). The assimilation of infrared atmospheric sounding interferometer radiances at ECMWF. *Quarterly Journal of the Royal Meteorological Society*, *135*(641), 1044–1058. https://doi.org/10.1002/qj.410

Cucurull, L., Anthes, R. A., & Tsao, L. L. (2014). Radio occultation observations as anchor observations in numerical weather prediction models and associated reduction of bias corrections in microwave and infrared satellite observations. *Journal of Atmospheric and Oceanic Technology*, *31*(1), 20–32. https://doi.org/10.1175/JTECH-D-13-00059.1

De Luccia, F., Guenther, B., Moeller, C., Xiong, X., & Wolfe, R. (2011). NPP VIIRS pre-launch performance and SDR validation. In *International Geoscience and Remote Sensing Symposium (IGARSS) Proceedings* (pp. 24–29). Vancouver, Canada: IEEE.

Elvidge, C. D., Baugh, K. E., Zhizhin, M., & Hsu, F. C. (2013). Why VIIRS data are superior to DMSP for mapping nighttime lights. *Proceedings of the Asia-Pacific Advanced Network*, *35*, 62–69. https://doi.org/10.7125/APAN.35.7

Gladkova, I., Ignatov, A., Shahriar, F., Kihai, Y., Hillger, D., & Petrenko, B. (2016). Improved VIIRS and MODIS SST imagery. *Remote Sensing*, *8*(1), 79. https://doi.org/10.3390/rs8010079

Han, Y., Revercomb, H., Cromp, M., Gu, D., Johnson, D., Mooney, D., et al. (2013). Suomi NPP CrIS measurements, sensor data record algorithm, calibration and validation activities, and record data quality. *Journal of Geophysical Research: Atmospheres*, *118*, 12,734–12,748. https://doi.org/10.1002/2013JD020344

Hillger, D., Kopp, T., Lee, T., Lindsey, D., Seaman, C., Miller, S., et al. (2013). First-light imagery from Suomi NPP VIIRS. *Bulletin of the American Meteorological Society*, *94*(7), 1019–1029. https://doi.org/10.1175/BAMS-D-12-00097.1

Hutchison, K. D., Iisager, B. D., & Hauss, B. (2012). The use of global synthetic data for pre-launch tuning of the VIIRS cloud mask algorithm. *International Journal of Remote Sensing*, *33*(5), 1400–1423. https://doi.org/10.1080/01431161.2011.571299

Joo, S., Eyre, J., & Marriott, R. (2013). The impact of Metop and other satellite data within the Met Office global NWP system using an adjoint-based sensitivity method. *Monthly Weather Review*, *141*(10), 3331–3342. https://doi.org/10.1175/MWR-D-12-00232.1

Kopp, T. J., Thomas, W., Heidinger, A. K., Botambekov, D., Frey, R. A., Hutchison, K. D., et al. (2014). The VIIRS Cloud Mask: Progress in the first year of S-NPP toward a common cloud detection scheme. *Journal of Geophysical Research: Atmospheres*, *119*, 2441–2456. https://doi.org/10.1002/2013JD020458

Li, J., Menzel, W. P., Sun, F., Schmit, T. J., & Gurka, J. (2004). AIRS subpixel cloud characterization using MODIS cloud products. *Journal of Applied Meteorology*, *43*(8), 1083–1094. https://doi.org/10.1175/1520-0450(2004)043%3C1083:ASCCUM%3E2.0.CO;2

Li, Y., Wu, A., & Xiong, X. (2016). Inter-comparison of S-NPP VIIRS and Aqua MODIS thermal emissive bands using hyperspectral infrared sounder measurements as a transfer reference. *Remote Sensing*, *8*(1), 72. https://doi.org/10.3390/rs8010072

Liang, X., & Ignatov, A. (2013). AVHRR, MODIS, and VIIRS radiometric stability and consistency in SST bands. *Journal of Geophysical Research: Oceans*, *118*, 3161–3171. https://doi.org/10.1002/jgrc.20205

Liu, Q., Cao, C., & Weng, F. (2013). Assessment of Suomi National Polar-Orbiting Partnership VIIRS emissive band calibration and inter-sensor comparisons. *IEEE Journal of Selected Topics in Applied Earth Observations and Remote Sensing*, *6*(3), 1737–1748. https://doi.org/10.1109/JSTARS.2013.2263197

Lu, J., Guo, J., Yang, L., Feng, T., & Zhang, J. (2016). Research and application of fire forecasting model for electric transmission lines incorporating meteorological data and human activities. *Mathematical Problems in Engineering*, *2016*(2), 1–10. https://doi.org/10.1155/2016/9828676

Madhavan, S., Brinkmann, J., Wenny, B. N., Wu, A., & Xiong, X. (2016). Evaluation of VIIRS and MODIS thermal emissive band calibration stability using ground target. *Remote Sensing*, *8*(2), 158. https://doi.org/10.3390/rs8020158

Moeller, C., Tobin, D., & Quinn, G. (2013). S-NPP VIIRS thermal band spectral radiance performance through 18 months of operation on-orbit. In *Proc. SPIE* (Vol. 8866, p. 88661N). https://doi.org/10.1117/12.2023389, http://spie.org/Publications/Proceedings/Paper/10.1117/12.2023389

Nagle, F. W., & Holz, R. E. (2009). Computationally efficient methods of collocating satellite, aircraft, and ground observations. *Journal of Atmospheric and Oceanic Technology*, *26*(8), 1585–1595. https://doi.org/10.1175/2008JTECHA1189.1

National Aeronautics and Space Administration (2013). Joint Polar Satellite System (JPSS) VIIRS Cloud Mask (VCM) AlgorithmTheoretical Basis Document (ATBD), Version B. Retrieved from http://npp.gsfc.nasa.gov/science/sciencedocuments/474-00033_ATBD-VIIRS-Cloud_Mask_B.pdf

Strow, L. L., Motteler, H., Tobin, D., Revercomb, H., Hannon, S., Buijs, H., et al. (2013). Spectral calibration and validation of the Cross-track Infrared Sounder on the Suomi NPP satellite. *Journal of Geophysical Research: Atmospheres*, *118*, 12,486–12,496. https://doi.org/10.1002/2013JD020480

Tobin, D., Holz, R., Nagle, F., & Revercomb, H. (2016). Characterization of the Climate Absolute Radiance and Refractivity Observatory (CLARREO) ability to serve as an infrared satellite intercalibration reference. *Journal of Geophysical Research: Atmospheres*, *121*, 4258–4271. https://doi.org/10.1002/2016JD024770

Tobin, D., Revercomb, H., Knuteson, R., Best, F., Taylor, J., Deslover, D., et al. (2013). The Cross-track Infrared Sounder (CrIS) on SUOMI NPP: Intercalibration with AIRS, IASI, and VIIRS. 93rd AMS Annual Meeting. Austin, TX.

Tobin, D., Revercomb, H., Knuteson, R., Taylor, J., Best, F., Borg, L., et al. (2013). Suomi-NPP CrIS radiometric calibration uncertainty. *Journal of Geophysical Research: Atmospheres*, *118*, 10,589–10,600. https://doi.org/10.1002/jgrd.50809

Wang, L., Han, Y., Jin, X., Chen, Y., & Tremblay, D. A. (2015). Radiometric consistency assessment of hyperspectral infrared sounders. *Atmospheric Measurement Techniques*, *8*(11), 4831–4844. https://doi.org/10.5194/amt-8-4831-2015

Wang, L., Han, Y., Tremblay, D., & Goldberg, M. (2012). Post-launch Radiometric and Spectral Calibration Assessment of NPP/CrIS by Comparing CrIS with VIIRS, AIRS, and IASI. 2012 Conference on Characterization and Radiometric Calibration for Remote Sensing.

Wang, L., Tremblay, D., Zhang, B., & Han, Y. (2016). Fast and accurate collocation of the Visible Infrared Imaging Radiometer Suite measurements with Cross-Track Infrared Sounder. *Remote Sensing*, *8*(1), 76. https://doi.org/10.3390/rs8010076

Wang, L., Tremblay, D. A., Han, Y., Esplin, M., Hagan, D. E., Predina, J., et al. (2013). Geolocation assessment for CrIS sensor data records. *Journal of Geophysical Research: Atmospheres*, *118*, 12,690–12,704. 704. https://doi.org/10.1002/2013JD020376

Wang, L., Zhang, B., Tremblay, D., & Han, Y. (2017). Improved scheme for Cross-track Infrared Sounder geolocation assessment and optimization. *Journal of Geophysical Research: Atmospheres*, *122*, 519–536. https://doi.org/10.1002/2016JD025812

Wang, P., Li, J., Li, Z., Lim, A. H., Li, J., Schmit, T. J., & Goldberg, M. D. (2017). The impact of Cross-track Infrared Sounder (CrIS) cloud-cleared radiances on Hurricane Joaquin (2015) and Matthew (2016) forecasts. *Journal of Geophysical Research: Atmospheres*, *122*, 13,201–13,218. https://doi.org/10.1002/2017JD027515

Xiong, X., Butler, J., Chiang, K., Efremova, B., Fulbright, J., Lei, N., et al. (2014). VIIRS on-orbit calibration methodology and performance. *Journal of Geophysical Research: Atmospheres*, *119*, 5065–5078. https://doi.org/10.1002/2013JD020423

Xiong, X., Butler, J., Chiang, K., Efremova, B., Fulbright, J., Lei, N., et al. (2016). Assessment of S-NPP VIIRS on-orbit radiometric calibration and performance. *Remote Sensing*, *8*(2), 84. https://doi.org/10.3390/rs8020084

Yang, J., Zhang, Z., Wei, C., Lu, F., & Guo, Q. (2017). Introducing the new generation of Chinese geostationary weather satellites–FengYun 4 (FY-4). *Bulletin of the American Meteorological Society*, *98*(8), 1637–1658. https://doi.org/10.1175/BAMS-D-16-0065.1

Zavyalov, V., Esplin, M., Scott, D., Esplin, B., Bingham, G., Hoffman, E., et al. (2013). Noise performance of the CrIS instrument. *Journal of Geophysical Research: Atmospheres*, *118*, 13,108–13,120. https://doi.org/10.1002/2013JD020457

Zavyalov, V., Fish, C. S., Bingham, G. E., Esplin, M., Greenman, M., Scott, D., & Han, Y. (2011). Preflight assessment of the cross-track infrared sounder (CrIS) performance. In *Proc. SPIE Europe: Atmospheric Remote sensing* (Vol. 8176, pp. 817606). Prague, Czech Republic, September 19–22 2011.

Zhou, L., Divakarla, M., & Liu, X. (2016). An overview of the Joint Polar Satellite System (JPSS) science data product calibration and validation. *Remote Sensing*, *8*(2), 139. https://doi.org/10.3390/rs8020139